Heliyon 9 (2023) e23093

Contents lists available at ScienceDirect

Heliyon

journal homepage: www.cell.com/heliyon

Rafting and redissolution of γ' phase in Ni–Al alloy under external stress

Jiajia Chen [a,1], Shenglong Wang [a,b,1], Kunwu Lai [a,b], Shuaige Yang [a,b], Zhichen Geng [a], Keyi Lin [a], Peng Sang [a,b], Qingqing Qin [a,b], Yongsheng Li [a,b,*]

[a] School of Materials Science and Engineering, Nanjing University of Science and Technology, Nanjing, China
[b] MIIT Key Laboratory of Advanced Metallic and Intermetallic Materials Technology, Nanjing, China

ARTICLE INFO

Keywords:
Ni-based superalloys
γ'phase
Stress
Redissolution
Kinetics

ABSTRACT

The volume fraction and rafting degree of the γ'-Ni_3Al phase under stress and high temperature are the key characteristics of mechanical properties in Ni-based superalloys, the rafting and redissolution of γ' phase caused by the creep at high temperature damage the morphology and properties of Ni-based superalloys. The phase-field simulation is performed to study the rafting accompany with the redissolution of γ' phase under high temperature and loading stress in Ni–Al alloy, the driving force and kinetics evolution of the γ' rafting were revealed. During the rafting under continuous heating, the elastic energy in the vertical γ channel is different to that of the horizontal γ channel, this difference in elastic energy drives the elements diffusion directionally to form the γ' rafts morphology. With the increased tensile stress, the decrease of specific surface of the γ' phase slows down the redissolution, a higher volume fraction is reserved for the rafted γ' phase. With temperature increases, the interface of γ/γ' phase becomes more diffusional and wider under stress. The results give an insight on the rafting mechanism of γ' phase and the kinetics evolution in Ni-based superalloys under excess temperature.

1. Introduction

Ni-based superalloys show the excellent mechanical properties and microstructure stability at elevated temperatures [1–4], therefore, these superalloys are served in the aero-engines or gas turbines. The good mechanical properties in Ni-based superalloys come from the precipitation strength of γ'-Ni_3Al precipitates embedded in the γ matrix. Shi et al. [5] found that the microhardness of the Ni-based alloy increases as the increased content of γ' phase, while the microhardness declines for the coarsening of γ' phase. Therefore, the morphology, size and volume fraction of γ' phase are key factors in the strengthening of Ni-based superalloys [6–8]. In the Ni-based superalloys, the γ' phase usually has a cubic shape and arranges in crystal directions [001] and [100], the γ' phase embedded in γ matrix can hinder the dislocation movement, thus can improve the mechanical properties [9,10]. However, after long-term exposure at high temperature, the cubic γ' phase will transform into ellipse by redissolution, resulting in the deterioration of mechanical properties [11–13]. Therefore, the morphology of γ' phase under various temperature and loading conditions were studied in Ni-based superalloys [14–16].

* Corresponding author. School of Materials Science and Engineering, Nanjing University of Science and Technology, Nanjing, China.
E-mail address: ysli@njust.edu.cn (Y. Li).
[1] These authors contributed equally to this work.

https://doi.org/10.1016/j.heliyon.2023.e23093
Received 7 April 2023; Received in revised form 22 November 2023; Accepted 27 November 2023
Available online 30 November 2023

The morphology change of the γ' phase in the heating process under stress is a critical question for the superalloys working at high temperatures. Yan et al. studied the morphology of γ' phases at creep state 1070 °C/137 MPa, the increasing in creep stress and overheating temperature reduce the creep life of the single crystal nickel-based superalloy, the results show that the dislocations shear into the rafted γ' phase in the later stage of creep [17]. In Coakley's work [18], the lattice strains and volume fraction were measured at creep state of 1150 °C and 100 MPa, the results showed a rapid decline in γ' volume fraction for the partially relieving of the lattice misfit. Xu et al. discovered the selective distribution of refractory elements and the effect on weakening the solution-strengthening and creep performance in Ni-based superalloy [19]. Xing et al. found that the overheating can induce the dissolution of γ' phases and the γ/γ' eutectic [20]. However, the evolution kinetics of the γ' phase during redissolution is still unclear with the continuous heating and external stress.

The redissolution of the cubic γ' phase was studied in process of continuous heating under external stress by the phase-field simulation. The evolution of composition, morphology, volume fraction, and size of the γ' phase were presented with different stresses, the effects of external stress on the diffusion of solute atoms and the stability of the γ' phase were revealed. In addition, the width variation of the γ/γ' phase interface was clarified during the redissolution of the γ' phase.

2. Model and methods

The composition field $c(\mathrm{r},t)$ is used to delegate the elements distribution, and long-range order (LRO) parameter fields $\eta_i(\mathrm{r},t)$ ($i=1$, 2, 3) are used to simulate the structure evolution of the γ' phase, where r is the three dimensional space and the t is time. The evolutions of the composition field and the LRO parameters are given by the Cahn-Hilliard and Ginzburg-Landau equations [21],

$$\frac{\partial c(\mathrm{r},t)}{\partial t}=\nabla\cdot\left[M_c\nabla\frac{\partial E_{\mathrm{total}}}{\partial c(\mathrm{r},t)}\right]+\xi_c(\mathrm{r},t) \tag{1}$$

$$\frac{\partial \eta_i(\mathrm{r},t)}{\partial t}=-M_\eta\frac{\partial E_{\mathrm{total}}}{\partial \eta_i(\mathrm{r},t)}+\xi_i(\mathrm{r},t)\quad(i=1,2,3) \tag{2}$$

where M_c and M_η are chemical and interface mobility, respectively, $\xi_c(\mathrm{r},t)$ and $\xi_i(\mathrm{r},t)$ are thermal noise in composition and LRO parameters, respectively. The thermal noise are used to induce the nucleation, and satisfy the fluctuation-dissipation theorem [22]. E_{total} is the total free energy and given in Eq. (3),

$$E_{\mathrm{total}}=\int_V\left[f(c,\eta_i)+\frac{\alpha}{2}(\nabla c)^2+\sum_{i=1}^{3}\frac{\beta}{2}(\nabla\eta_i)^2+E_{\mathrm{el}}\right]dV \tag{3}$$

where V is the volume, $f(c,\eta_i)$ is the chemical free energy density. E_{el} is the elastic strain energy density, α and β are respectively gradient energy coefficients of composition and order parameters. The Gibbs free energy $g(c,\eta_i)$ in Eq. (4) can be express by $g(c,\eta_i)=f(c,\eta_i)\cdot V_m$ [23], where V_{m} is the molar volume.

$$g(c,\eta_i)=g^{\gamma}(c)+g^{\gamma'}(c,\eta_i)-g^{\gamma'}(c,\eta_i=0)\quad(i=1,2,3) \tag{4}$$

where g^{γ} and $g^{\gamma'}$ are the Gibbs free energies of the γ phase and γ' phase respectively, and can be given by Eqs. (5) and (6),

$$g^{\gamma}=g_0^{\gamma}+\Delta g_{ideal}^{\gamma}+\Delta g_{xs}^{\gamma}+\Delta g_{mag}^{\gamma} \tag{5}$$

$$g^{\gamma'}=g_0^{\gamma'}+\Delta g_{ideal}^{\gamma'}+\Delta g_{xs}^{\gamma'} \tag{6}$$

where g_0^{γ}, $\Delta g_{ideal}^{\gamma}$, Δg_{xs}^{γ}, Δg_{mag}^{γ}, $g_0^{\gamma'}$, $\Delta g_{ideal}^{\gamma'}$ and $\Delta g_{xs}^{\gamma'}$ are given in Eqs. (7) − (13),

$$g_0^{\gamma}=cg_0^{\mathrm{Al}}+(1-c)g_0^{\mathrm{Ni}} \tag{7}$$

$$\Delta g_{ideal}^{\gamma}=RT[c\ln c+(1-c)\ln(1-c)] \tag{8}$$

$$\Delta g_{xs}^{\gamma}=c(1-c)\left[L_0+L_1(2c-1)+L_2(2c-1)^2+L_3(2c-1)^3\right] \tag{9}$$

$$\Delta g_{mag}^{\gamma}=RT\ln(\mu+1)f(\tau) \tag{10}$$

$$g_0^{\gamma'}=6U_1c^2\sum_{i=1}^{3}\eta_i^2 \tag{11}$$

$$\Delta g_{ideal}^{\gamma'} = (RT/4)\times\left\{\begin{array}{l}[c(1+\eta_1+\eta_2+\eta_3)]\ln[c(1+\eta_1+\eta_2+\eta_3)]\\+[1-c(1+\eta_1+\eta_2+\eta_3)]\ln[1-c(1+\eta_1+\eta_2+\eta_3)\\+[c(1-\eta_1-\eta_2+\eta_3)]\ln[c(1-\eta_1-\eta_2+\eta_3)]\\+[1-c(1-\eta_1-\eta_2+\eta_3)]\ln[1-c(1-\eta_1-\eta_2+\eta_3)\\+[c(1-\eta_1+\eta_2-\eta_3)]\ln[c(1-\eta_1+\eta_2-\eta_3)]\\+[1-c(1-\eta_1+\eta_2-\eta_3)]\ln[1-c(1-\eta_1+\eta_2-\eta_3)\\+[c(1+\eta_1-\eta_2-\eta_3)]\ln[c(1+\eta_1-\eta_2-\eta_3)]\\+[1-c(1+\eta_1-\eta_2-\eta_3)]\ln[1-c(1+\eta_1-\eta_2-\eta_3)\end{array}\right\} \tag{12}$$

$$\Delta g_{xs}^{\gamma'} = -2U_1c^2\sum_{i=1}^{3}\eta_i{}^2+12U_4(1-2c)c^2\sum_{i=1}^{3}\eta_i{}^2-48U_4c^3\eta_1\eta_2\eta_3 \tag{13}$$

By using the thermodynamic database of CALPHAD, the total Gibbs energy of the Ni–Al alloy is given in Eq. (14) [23,24].

$$\begin{aligned}g(c,\eta_1,\eta_2,\eta_3) &= cg_0^{\mathrm{Al}}+(1-c)g_0^{\mathrm{Ni}}+RT\ln(\mu+1)f(\tau)+c(1-c)\left[L_0+L_1(2c-1)+L_2(2c-1)^2+L_3(2c-1)^3\right]\\&+4U_1c^2\sum_{i=1}^{3}\eta_i{}^2+12U_4(1-2c)c^2\sum_{i=1}^{3}\eta_i{}^2-48U_4c^3\eta_1\eta_2\eta_3\\&+(RT/4)\times\left\{\begin{array}{l}[c(1+\eta_1+\eta_2+\eta_3)]\ln[c(1+\eta_1+\eta_2+\eta_3)]\\+[1-c(1+\eta_1+\eta_2+\eta_3)]\ln[1-c(1+\eta_1+\eta_2+\eta_3)\\+[c(1-\eta_1-\eta_2+\eta_3)]\ln[c(1-\eta_1-\eta_2+\eta_3)]\\+[1-c(1-\eta_1-\eta_2+\eta_3)]\ln[1-c(1-\eta_1-\eta_2+\eta_3)\\+[c(1-\eta_1+\eta_2-\eta_3)]\ln[c(1-\eta_1+\eta_2-\eta_3)]\\+[1-c(1-\eta_1+\eta_2-\eta_3)]\ln[1-c(1-\eta_1+\eta_2-\eta_3)\\+[c(1+\eta_1-\eta_2-\eta_3)]\ln[c(1+\eta_1-\eta_2-\eta_3)]\\+[1-c(1+\eta_1-\eta_2-\eta_3)]\ln[1-c(1+\eta_1-\eta_2-\eta_3)\end{array}\right\}\end{aligned} \tag{14}$$

where g_0^{Ni} and g_0^{Al} are the Gibbs energy of pure Ni and Al, respectively, L_0, L_1, L_2 and L_3 are interaction parameters. U_1 and U_4 are bond energy parameters. R is the gas constant, T is the absolute temperature. μ= 0.52 is the average value of atomic magnetic moment, and $f(\tau)$ is a function related to it. These inputs are referred in CALPHAD database [25–27].

The elastic strain energy density is written as Eq. (15) [28,29].

$$E_{\mathrm{el}} = 1/2C_{ijkl}\varepsilon_{ij}^{\mathrm{el}}\varepsilon_{kl}^{\mathrm{el}} \tag{15}$$

where C_{ijkl} is the elastic constant tensor. The elastic strain is given by $\varepsilon_{ij}^{\mathrm{el}} = \varepsilon_{ij}^{\mathrm{a}}+\varepsilon_{ij}-\varepsilon_{ij}^{0}$, where $\varepsilon_{ij}^{\mathrm{a}}$ is the strain induced by applied stress, ε_{ij} is the internal strain, the eigenstrain $\varepsilon_{ij}^{0} = \varepsilon_0\delta_{ij}\delta_c$, where $\varepsilon_0 = (1/a)(da/dc)$ with a is lattice parameter and c is the composition, δ_{ij} is the Kronecker delta function, and $\delta_c = c-c_0$ with c_0 being the nominal composition. The lattice parameter a and the elastic constants of Ni–Al alloy vary with the temperature [30].

The dimensionless parameters are introduced to solve Eqs. (1) and (2), $\nabla^* = \partial/\partial(\mathrm{r}/l)$, $\chi = M_c/M_\eta l^2$, $\alpha^* = \alpha/l^2|\Delta f|$, $\beta^* = \beta/l^2|\Delta f|$, $E^* = E_{el}/|\Delta f|$, $f^*(c,\eta_i) = f(c,\eta_i)/|\Delta f|$, $t^* = tM_\eta|\Delta f|$. Where $|\Delta f|$= 3.3×10^{7}Jm^{-3} [31] and l = 1.5 nm is the length scale. χ = 0.0004, M_η= 5.8×10^{-9}m^{3}J^{-1}s^{-1} [32]. The grid length is Δx^*= Δy^*= 0.3 with the grid number of 256, the time step is Δt^* = 0.0005.

The semi-implicit Fourier-spectral is adopted to solve the dimensionless equations [33]. The parameters α= 2.5×10^{-9}Jm^{-1} and α= 2.524×10^{-9}Jm^{-1} at 1000 K and 1300 K respectively, and the β= 6.0×10^{-12}Jm^{-1} and β = 7.29 × 10^{-12}Jm^{-1}, respectively [23,34]. We adopt the α= 2.5×10^{-9}Jm^{-1} and β = 6.0 × 10^{-12}Jm^{-1}. The thermal fluctuations for composition is [−0.001, 0.001], and for order parameters is [−0.002, 0.002].

The stress is calculated by the Hooke's law $\sigma_{ij} = C_{ijkl}\varepsilon_{kl}$ and the equivalent stress formula $\sigma_{xx} = \sqrt{0.5\times(\sigma_{11}-\sigma_{22})^2+3\sigma_{12}^2}$ [35], where the σ_{11}, σ_{22} and σ_{12} are the stresses in fcc structure. The elastic constants of γ′ precipitate and γ matrix are implemented as $C_{11}^{\gamma'}$ = 236.7 GPa, $C_{12}^{\gamma'}$ = 142.0 GPa, $C_{44}^{\gamma'}$ = 100.6 GPa and C_{11}^{γ} = 215.5 GPa, C_{12}^{γ} = 164.2 GPa, C_{44}^{γ} = 77.6 GPa.

3. Results and discussion

3.1. Evolution of γ' phase under stress during isothermal aging

The previous study shown that the elastic strain energy drives the redistribution of elements between the γ and γ' phases, which becomes obvious under external stress [36]. Fig. 1 (a) shows the two-dimensional morphology of the Ni-17 at.% Al alloy at 973 K and t^* = 100, where the red color delegates the γ' phase and the blue color delegates the γ phase. Under the tensile stresses σ_{xx} = 212 MPa and σ_{xx} = 424 MPa, the cubic γ' phase is elongated and connected into strip-shape in direction [10], as shown in Fig. 1(c) and (d), which

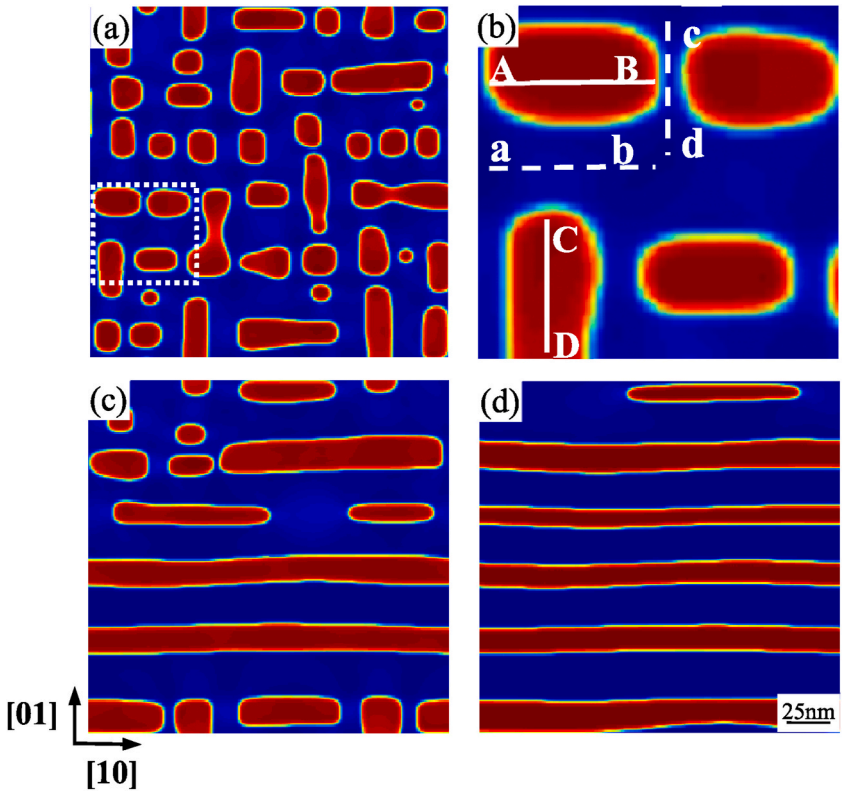

Fig. 1. Isothermal aging and rafted morphology of γ' phase in Ni-17 at.% Al alloy at 973 K, (a) $t^* = 100$, $\sigma_{xx} = 0$ MPa, (b) The local amplification of graphic (a), (c) $t^* = 250$, $\sigma_{xx} = 212$ MPa, (d) $t^* = 250$, $\sigma_{xx} = 424$ MPa.

is called as the rafting or directional coarsening in single crystal superalloys, here the *P*-type rafting happens in the Ni-17 at.% Al alloy, i.e. the rafting direction of γ' phase is parallel to the stress direction. It can be seen from Fig. 1(c) and (d) that the rafting degree of γ' phase is more obvious for a large stress $\sigma_{xx} = 424$ MPa. Yan et al. found that the γ' phase is rafted under creep state 1070 °C/137 MPa in Ni-based superalloys [17]. Coakley et al. studied the precipitates in nickel-based superalloys under tensile creep, their results shown that the raft is formed at 1150 °C/100 MPa [18]. Our simulation results in γ' morphology are similar with the previous experiment.

3.1.1. Driving force of diffusion under external stress

Mughrabi et al. [37,38], Nabarro et al. [39] and Socrate et al. [40] declared that the external stress causes the strain energy to accumulate in the horizontal or vertical channels of γ matrix, thereby forming an elastic strain energy gradient that drives the solute atom to migrate between the horizontal and vertical channels, which produces the rafting morphology of the γ' phase. Mughrabi showed that the redistribution of Al atoms in the boundary region of γ/γ' phases to form the rafting morphologies affected by tensile stress [37]. For example, the elastic strain energy in γ channel is low at the middle of segments a-b and c-d (see Fig. 1(b)), as signed by letter F and G in Fig. 2(a), these positions lie in the central line of two neighbor γ' phases. While both ends of the a-b and c-d segments have large values, such as position E. The Al content at both ends of the segments a-b and c-d are lower than the central areas, as shown

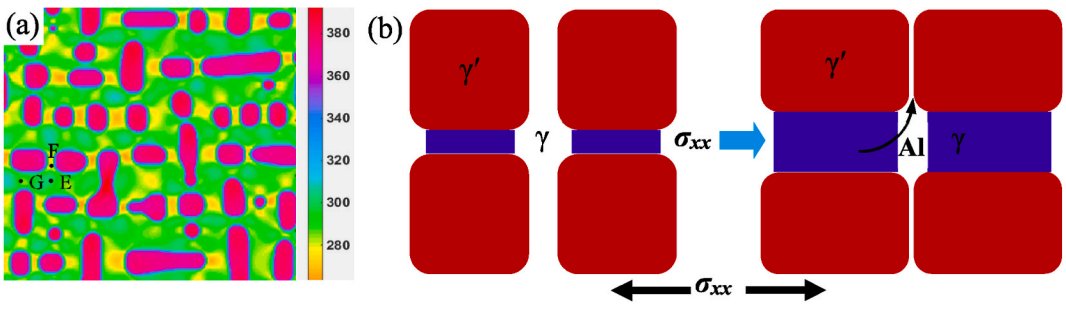

Fig. 2. (a) Distribution of elastic strain energy in γ and γ' phase under $\sigma_{xx} = 212$ MPa , (b) schematic of Al diffusion in the γ channel under tensile stress along horizontial direction.

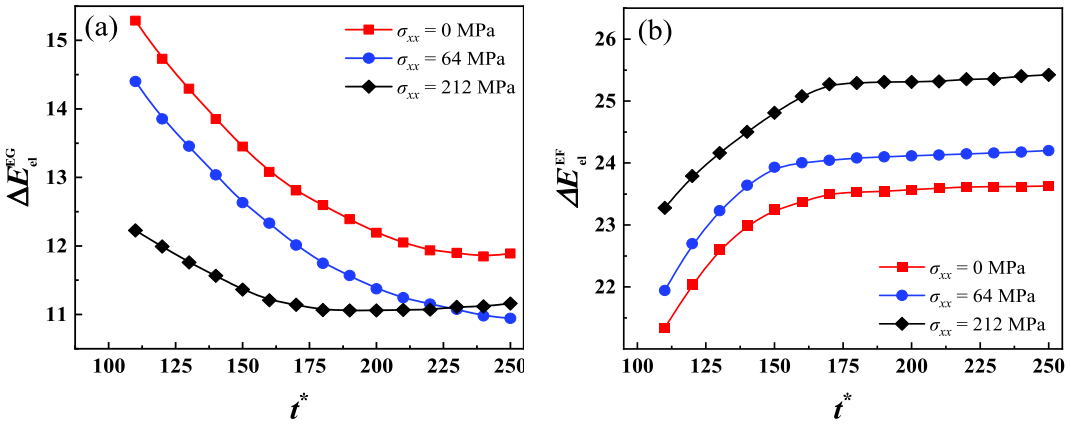

Fig. 3. Difference of elastic energy in the horizontal and vertical γ channels under tensile stress, (a) ΔE_{el}^{EG}, (b) ΔE_{el}^{EF}.

in Fig. 5, which means that Al diffuses from the position E with higher strain energy to the positions of low strain energy in the rafting process.

Fig. 2(b) gives a schematic of directional diffusion of Al in the γ channel under external stress σ_{xx}, where the blue regions delegate the horizontal channel with high strain energy. The γ' phase dissolves from the boundary of horizontal channel, the Al migrates from the horizontal to the vertical channels, therefore, the horizontal channel becomes wider and the vertical channel becomes narrower, the horizontal connection of γ' phase and the *P*-type rafting is formed.

Fig. 3 shows the variations difference in strain energy, ΔE_{el}, between positions E and G, E and F(see Fig. 2(a)), which are defined as ΔE_{el}^{EG} and ΔE_{el}^{EF}, respectively. As shown in Fig. 3(a) and (b), the ΔE_{el}^{EG} becomes small as the increase of time and tensile stress, while ΔE_{el}^{EF} becomes large. The changes of elastic energy difference ΔE_{el}^{EG} in horizontal and ΔE_{el}^{EF} in vertical channel of γ matrix indicates that the Al atoms diffuse from horizontal to vertical channel. Therefore, the gradient of elastic strain energy drives the diffusion of element to form the rafted morphology.

3.1.2. Composition inhomogeneity in γ and γ' phase

The Al contents in γ' phase along the direction [10] in A-B segment and direction [01] in C-D segment (see Fig. 1(b)) under tensile stress are shown in Fig. 4. As the tensile stress increases, the Al content increases in the direction [10] (A-B segment), and the Al content in the middle of γ' phase becomes higher than that in the boundary region, such as σ_{xx} = 424 MPa in Fig. 4(a). During the rafting process, the γ' phase absorbs the Al atom at both ends of the γ' phase particles, such as positions A and B, where has an instantaneous low concentration under high stress σ_{xx} = 318 MPa and σ_{xx} = 424 MPa. In the [01] direction (C-D segment), the Al content decreases with the tensile stress increasing, and the middle concentration becomes lower than that of the two ends, as shown in Fig. 4(b).

Because of the Al in the horizontal γ channels migrate into the vertical channels, the Al content in the horizontal γ channels becomes small with the increased external stress, as shown in Fig. 5(a), while the Al content in the vertical channels increases with the tensile stress increase, as shown in Fig. 5(b). Under the external stress, the elastic strain energy gradient is rapidly established in the γ channels, so the Al in the γ channel rapidly diffuses to the vertical channel under the elastic energy gradient. In addition, the difference of Al content between the middle and both ends of the horizontal matrix channel decreases as the tensile stress increases, the difference

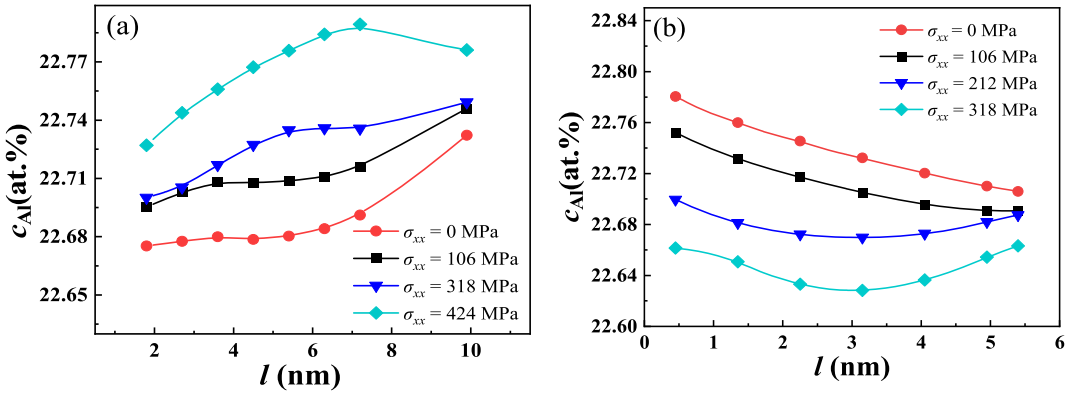

Fig. 4. Al content c_{Al} evolution in γ' phases along the horizontal and vertical directions under tensile stress at t^* = 300, (a) A-B segment, (b) C-D segment.

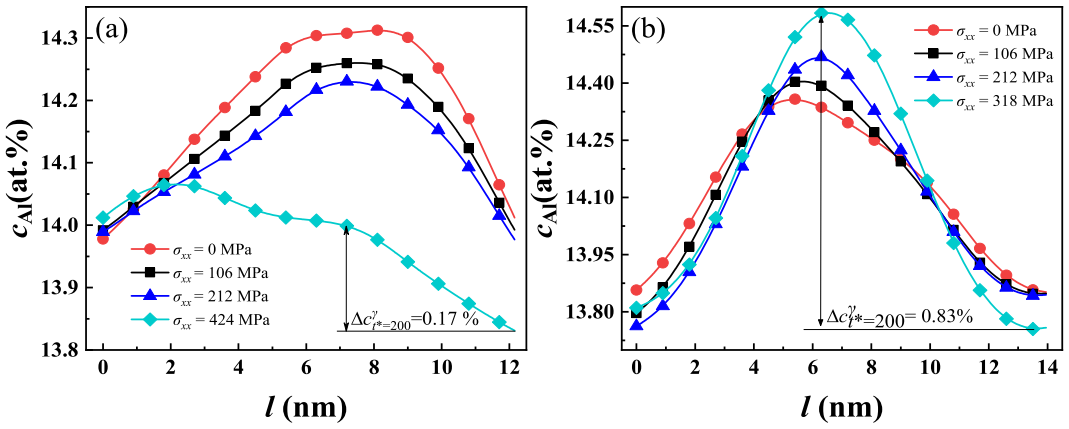

Fig. 5. Evolution of Al content c_{Al} in γ channels of region An under tensile stresses at $t^* = 300$, (a) a-b segment, (b) c-d segment.

of Al content $\Delta c^{\gamma}_{t*=200} = 0.17$ % for $\sigma_{xx} = 424$ MPa, as shown in Fig. 5(a), while in the vertical channel, the difference of Al content $\Delta c^{\gamma}_{t*=200}$ increases with tensile stress, the difference of Al content is $\Delta c^{\gamma}_{t*=200} = 0.83$ % for $\sigma_{xx} = 318$ MPa.

It should be noting that the difference of composition between the center and end of the a-b and c-d segments (see Fig. 1(b)) in γ channels are both larger than that of the A-B and C-D segments of γ' phase, as shown in Figs. 4 and 5.

3.2. *Redissolution of γ' phase under stress*

The morphology of γ' phase with different heating rates and tensile stresses is illustrated in Fig. 6, where Fig. 6(a) shows the aged morphology at 973 K for $t^* = 100$ without external stress. When the temperature increases to 1255 K with a heating rate $k = 6$, some γ' particles with small size are dissolved in Fig. 6(b). Under the tensile stress $\sigma_{xx} = 424$ MPa in Fig. 6(c), the γ' phases are elongated and some γ' phases with small size are dissolved. As the temperature increases to 1273 K, more γ' particles are dissolved in Fig. 6(d), the elongation of the γ' phase is continuous under tensile stress, as can be seen in Fig. 6 (e) and (f).

Lai et al. [11] found that the diffusion of Al is not uniformly after a short time of pre-aging. Because of the overlap of the diffusion fields, the diffusion of solute atoms causes the connection of adjacent γ' phase. The increased temperature promotes the diffusion, the adjacent γ' phase will be connected through the "diffusion neck". In addition, the external stress drives the solute atoms to diffuse

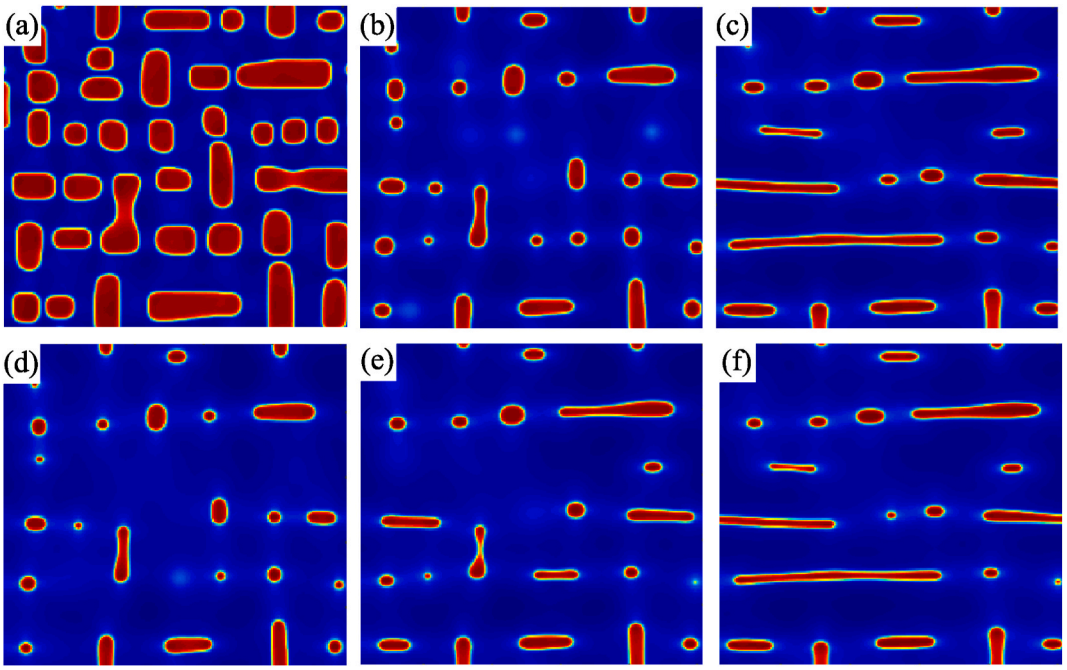

Fig. 6. Morphology evolutions of γ' phase in Ni-17.0 at.% Al alloy with tensile stress, (a) isothermal aged at 973 K for $t^* = 100$, $\sigma_{xx} = 0$ MPa, (b) $\sigma_{xx} = 0$ MPa, $T = 1255$ K, (c) $\sigma_{xx} = 424$ MPa, $T = 1255$ K, (d) $\sigma_{xx} = 0$ MPa, $T = 1273$ K, (e) $\sigma_{xx} = 212$ MPa, $T = 1273$ K, (f) $\sigma_{xx} = 424$ MPa, $T = 1273$ K.

directionally [41], which promotes the overlap of the diffusion fields and the formation of the "diffusion neck", so the connection of γ' phase is particularly obvious when the external stress is applied, which can be seen in Fig. 6(d) and (f).

3.3. Redissolution kinetics of γ' phase under stress

3.3.1. Evolution of volume fraction

Fig. 7(a) – (c) show the volume fraction of γ' phase with heating rates $k = 2$, 6 and 10 under the tensile stress. It is clearly that the γ' phase reaches a large volume fraction under large stress and large heating rate after redissolution. When heating to 1273 K, the difference of volume fraction between $\sigma_{xx} = 424$ MPa and $\sigma_{xx} = 0$ MPa are $\Delta V = 1.83$ %, 0.73 %, and 0.26 % for $k = 2$, 6 and 10, respectively. Therefore, with tensile stress increases, the lower heating rate produces the larger ΔV for the longer diffusion time. For the compressive stress in Fig. 7(d) – (f), the large stress $\sigma_{xx} = -424$ MPa produces a high volume fraction than that of $\sigma_{xx} = 0$ MPa for $k = 2$, as shown in Fig. 7(d). However, high heating rate $k = 10$ and large stress $\sigma_{xx} = -424$ MPa produce a lower volume fraction than that of $\sigma_{xx} = 0$ MPa, as shown in Fig. 7 (f). When the heating rate changes from $k = 2$ to 6 and 10, at 1273 K, the differences of volume fraction are $\Delta V = 0.24$ %, 0.20 %, and – 0.31 % for $\sigma_{xx} = -424$ MPa and $\sigma_{xx} = 0$ MPa.

For the low heating rate, it will go through a long time for heating to 1270 K, and the redissolution of γ' phase is slowly. In this process, the stress has more impact on the morphology, such as the connection of γ' phase reduces the redissolution, for a large size particle has a lower specific surface area (BET). When the temperature increases to 1273 K with rate $k = 2$, in state of stress-free $\sigma_{xx} = 0$ MPa, tensile stress $\sigma_{xx} = 212$ MPa and $\sigma_{xx} = 424$ MPa, the BETs of the γ' phase are 0.285 nm^{-1}, 0.283 nm^{-1} and 0.278 nm^{-1}, respectively. When the heating rate is $k = 6$, the BETs of the γ' phase under the three stresses are 0.358 nm^{-1}, 0.357 nm^{-1} and 0.350 nm^{-1}. For $k = 10$, the BETs are 0.374 nm^{-1}, 0.373 nm^{-1} and 0.371 nm^{-1}. With the increased heating rate, the BETs of γ' phase increase, while the BETs decrease with the increased tensile stress. The dissolution of γ' phase is affected by the diffusion across the phase interface [42]. The decrease of γ' phase BET slows down the diffusion rate of solute atoms, resulting in a slower redissolution of γ' phase. Therefore, the ΔV is reduced at a high heating rate in which the diffusion time is shorter. Ola et al. [43] have pointed out that compressive stress promotes the diffusion, while tensile stress inhibits the diffusion of atoms in IN738LC superalloy. This explains that the compressive stress produces small volume fraction of the γ' phase for a fast diffusion than that of the tensile stress.

3.3.2. Variations of average radius and particle number

Fig. 8 shows the change of the average particle radius $< r >$ of γ' phase with different tensile stresses during the redissolution process. The average radius is calculated by $< r > = \sqrt{A_\gamma / \pi N}$, where A_γ is the total area of the γ' phase particles in the two-dimensional graph, N is the number of γ' particles. It can be seen that the stress influences the particle size greatly for a lower heating rate $k = 4$, a large $< r >$ is presented for a larger stress $\sigma_{xx} = 424$ MPa, as shown in Fig. 8(a). This is because that the more γ' particles can be

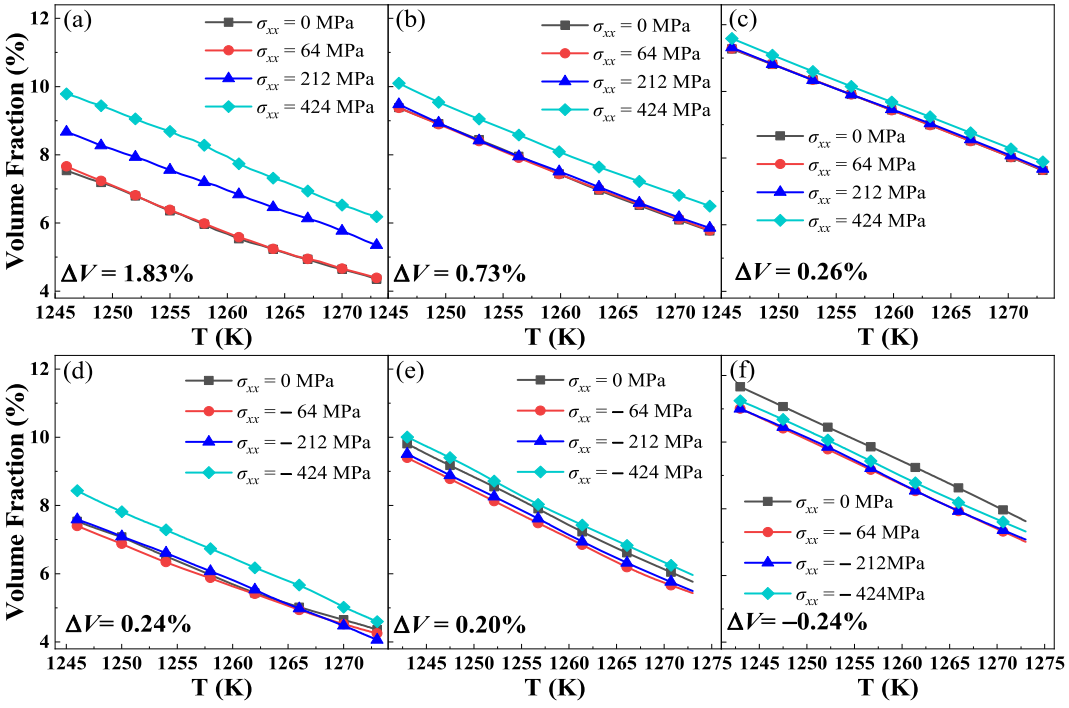

Fig. 7. Variations of γ' phase volume fraction with tensile stress in (a) – (c), (a) $k = 2$, (b) $k = 6$, (c) $k = 10$, and with compressive stress in (d) – (f), (d) $k = 2$, (e) $k = 6$, (f) $k = 10$.

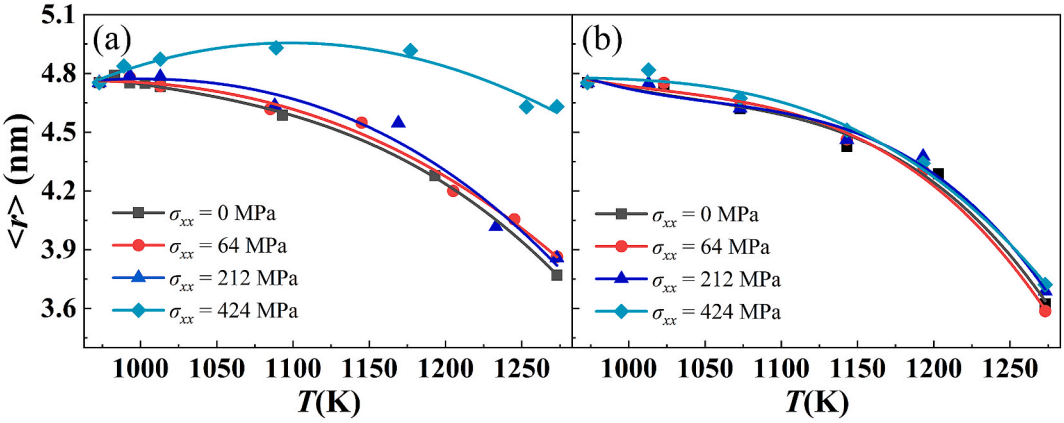

Fig. 8. Variations of average particle radius $< r >$ of γ' phase during redissolution with tensile stress and heating rate (a) $k = 4$, and (b) $k = 10$.

connected under the tensile stress in the early stage of heating. However, for the faster heating rate $k = 10$, the adjacent γ' phase particles have been dissolved before the interconnection happening, so the average radii are similar under different stresses, as shown in Fig. 8 (b).

3.3.3. *Variations of γ/γ' phase interfacial width*

During the continuous heating in Ni-based superalloys, the width of the composition interface of γ/γ' phase will be changed. The composition interfacial width is calculated with the method proposed by Woodward [44] and Seidman et al. [45], they defined the interfacial width as the distance corresponding to 90 % and 10 % of the average component height of the two phases. Fig. 9 shows the change of Al composition at the interface of γ/γ' phase at different temperatures during continuous heating under tensile stress $\sigma_{xx} =$ 424 MPa. The Al content in γ' phase declines from 22.72 at. % to 22.42 at. % with elevating temperature, while the Al content in the γ matrix increases from 14.20 at.% to 17.09 at.%, the composition variations are consistent with the Ni–Al phase diagram [46].

The variations of interfacial width δ with temperature are shown in Fig. 10. For $\sigma_{xx} = 0$ MPa, when temperature rises from 973 K to 1273 K, the interfacial width increases from $\delta = 1.37$ nm –1.45 nm ($k = 2$) and 1.56 nm ($k = 10$), and the difference between the two heating rates at 1273 K is $\Delta\delta = 0.11$ nm, which has the same rule with Ni–17 at.% Al alloy aging at 923, 973 and 1023 K [8]. The 3D-APT experiment also shows the similar interfacial width 1.22 – 1.58 nm in Ni-12.5 at.% Al and Ni-13.4 at.% Al alloy, aging at 823 and 873 K [47]. For the $k = 2$, the interfacial width increases from $\delta = 1.37$ nm – 1.49 nm and 1.63 nm under the tensile stress $\sigma_{xx} =$ 424 MPa and compressive stress $\sigma_{xx} = -424$ MPa, respectively, the $\Delta\delta = 0.14$ nm for tensile and compressive stress. Therefore, it can be deduced that the interfacial width increases with temperature rising in the process of continuous heating. The compressive stress makes the interface more diffusional and wide, which induces the strong rafting of the γ' phase during the continuous heating process.

In addition, during the rafting process, the increase of interfacial width in rafting direction is observed in creep experiment of a Ni-based single crystal superalloy for 100 h at 1100 °C/137 MPa, which is related to the redistribution of elements [48]. The stress promotes the diffusion of Al element to partition into γ′ phase from γ matrix during rafting, which widens the composition interface in rafting direction [29]. Therefore, phase field simulation gives a convincing result about the variation of interfacial width with the temperature rising for Ni–Al alloys.

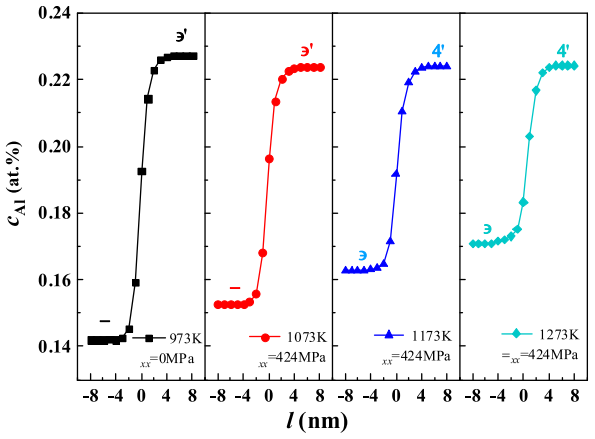

Fig. 9. Al composition profile of γ/γ' phase interface in the process of continuous heating with $k = 2$ and tensile stress $\sigma_{xx} = 424$ MPa.

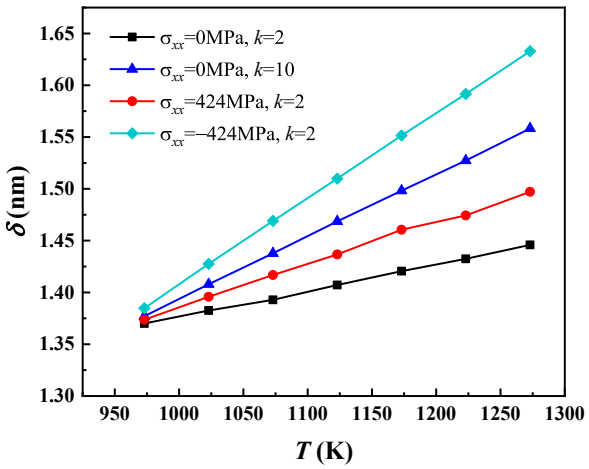

Fig. 10. Variation of γ/γ' phase composition interfacial width with temperature under stress.

4. Conclusions

The morphology and kinetics evolution during the redissolution of γ' phase in Ni-17 at.% Al alloy are clarified in state of continuous heating with external tensile stress. The effects of external stress on the Al diffusion are revealed during the redissolution and orientation alignment of γ′ phases. The difference of elastic strain energy raised from the vertical and horizontal γ channels induces the directional diffusion of elements to form the rafting morphology in isothermal aging. During the continuous heating process, the external stress σ_{xx} slows down the dissolution of γ' phase which arranged in the [10] direction, for the interconnection of adjacent γ' phase happens under stress. The connecting of γ' phase reduces the specific surface area of γ' phase, resulting in a low diffusion of Al and the dissolution rate of γ' phase. As the temperature increases, the composition interfacial width of γ/γ' phase increases in process of continuous heating. For the heating rate $k = 2$, the redistribution of elements widens the phase interface in rafting direction under external stress.

Data availability statement

Data will be made available on request.

Additional information

No additional information is available for this paper.

CRediT authorship contribution statement

Jiajia Chen: Writing - review & editing, Resources. **Shenglong Wang:** Writing - review & editing, Software. **Kunwu Lai:** Writing - original draft. **Shuaige Yang:** Writing - original draft. **Zhichen Geng:** Resources. **Keyi Lin:** Software. **Peng Sang:** Writing - original draft. **Qingqing Qin:** Investigation. **Yongsheng Li:** Writing - review & editing, Writing - original draft, Software, Resources, Conceptualization.

Declaration of competing interest

The authors declare that they have no known competing financial interests or personal relationships that could have appeared to influence the work reported in this paper.

Acknowledgements

This work was supported by the National Natural Science Foundation of China [Grant No. 52275342] and the Fundamental Research Funds for the Central Universities [Grant No. 30921013107].

References

[1] C. Edtmaier, M. Wolf, R.D.O. Calderon, W.D. Schubert, Effect of nickel on the formation of γ/γ' microstructures in WC/Co-Ni-Al-W, Int. J. Refract. Met. H. 100 (2021), 105652.

[2] H.Y. Wang, Y.S. Li, X.Y. Zhang, Z.H. Cheng, K.Y. Li, Composition distribution and kinetics evolution of γ' phase in Ni-(17-*x*)Al-*x*Mo (at.%) alloys, J. Mater. Res. Technol. 15 (2021) 561–571.
[3] J.G. Yu, S.M. Zhang, Q.X. Zhang, R. Liu, M.K. Tang, X.W. Li, Simulation study and experiment verification of the creep mechanism of a nickel-based single crystal superalloy obtained from microstructural evolution, RSC Adv. 6 (2016), 107748.
[4] E.Y. Plotnikov, Z.G. Mao, S.I. Baik, M. Yildirim, Y.S. Li, D. Cecchetti, R.D. Noebe, G. Martin, D.N. Seidman, Correlative four-dimensional study of phase-separation at the subnanoscale to nanoscale of a Ni-Al alloy, Acta Mater. 171 (2019) 306–333.
[5] S.J. Shi, C.W. Liu, Y.S. Li, S. Maqbool, X.Y. Zhang, M. Huang, Coarsening kinetics of γ' phase in isothermal aged high Al content Ni-17 at.% Al alloy, Mater. Chem. Phys. 271 (2021), 124902.
[6] X.C. Wu, Y.S. Li, M.Q. Huang, W. Liu, Z.Y. Hou, Precipitation kinetics of ordered γ' phase and microstructure evolution in a Ni-Al alloy, Mater. Chem. Phys. 182 (2016) 125–132.
[7] N. Khatavkar, S. Swetlana, A.K. Singh, Accelerated prediction of Vickers hardness of Co- and Ni-based superalloys from microstructure and composition using advanced image processing techniques and machine learning, Acta Mater. 196 (2020) 295–303.
[8] X.C. Wu, Y.S. Li, W. Liu, Z.Y. Hou, M.Q. Huang, Dynamics evolution of γ' precipitates size and composition interface between γ/γ' phase in Ni−Al alloy at different aging temperatures, Rare Met. 41 (2022) 3552–3559.
[9] D.M. Collins, H.J. Stone, A modelling approach to yield strength optimisation in a nickel-base superalloy, Int. J. Plasticity. 54 (2014) 96–112.
[10] M.Z. Li, J. Coakley, D. Isheim, G.F. Tian, B. Shollck, Influence of the initial cooling rate from γ' supersolvus temperatures on microstructure and phase compositions in a nickel superalloy, J. Alloys Compd. 732 (2018) 765–776.
[11] K.W. Lai, S.J. Shi, Z.W. Yan, S.S. Jin, D. Wang, Phase-field simulation of re-dissolution of γ' phase in Ni-Al alloy by continuous and second-order aging treatment, Rare Met. 40 (2021) 1155–1163.
[12] A. Epishin, T. Link, U. Bruchner, P.D. Portella, Kinetics of the topological inversion of the γ/γ'-microstructure during creep of a nickel-based superalloy, Acta Mater. 49 (2021) 4017–4023.
[13] L.Z. He, Q. Zheng, X. Sun, H.R. Guan, Z.Q. Hu, A.K. Tieu, C. Lu, H.T. Zhu, High-temperature creep-deformation behavior of the Ni-based superalloy M963, Metall. Mater. Trans. A. 36 (2005) 2385–2391.
[14] Y. Liu, J.M. Wu, Z.C. Zhi, X.G. Xiao, M. Avdeev, S.Q. Shi, C.Y. Wang, T. Yu, Predicting creep rupture life of Ni-based single crystal superalloys using divide-and-conquer approach based machine learning, Acta Mater. 195 (2020) 454–467.
[15] Y.S. Zhao, Y.S. Luo, M. Zhang, B. Gan, K.Q. Yuan, X.X. Wu, On the effect of Ru upon creep behaviour and dislocation evolution in Ni-based single crystal superalloys, Mater. Today Commun. 30 (2022), 103220.
[16] F. Touratier, E. Andrieu, D. Poquillon, B. Viguier, Rafting microstructure during creep of the MC2 nickel-based superalloy at very high temperature, Mat. Sci. Eng. A. 510 (2009) 244–249.
[17] H.J. Yan, S.G. Tian, G.Q. Zhao, S.K. Zhang, Creep damage of a high Mo single crystal nickelbased superalloy, Mater. High Temp. 37 (2020) 139–144.
[18] J. Coakley, D. Ma, M. Frost, D. Dye, D.N. Seidman, D.C. Dunand, H.J. Stone, Lattice strain evolution and load partitioning during creep of a Ni-based superalloy single crystal with rafted γ' microstructure, Acta Mater. 135 (2017) 77–87.
[19] R.D. Xu, Y. Li, H.C. Yu, Microstructure evolution and dislocation mechanism of a Third-Generation single-crystal Ni-based superalloy during creep at 1170°C, Materials 16 (2023), 5166.
[20] W.J. Xing, G. Zhu, X.L. Zuo, X.T. Guo, Z.B. Zhao, H. Xiao, Z. Zheng, W.X. Zhao, C.K. Liu, Abnormal creep property degradation in a directionally solidified superalloy DZ406 after suffering overheating, Mater. Charact. 173 (2021), 110910.
[21] Y. Wang, D. Banerjee, C.C. Su, A.G. Khachaturyan, Field kinetic model and computer simulation of precipitation of $L1_2$ ordered intermetallics from f.c.c. solid solution, Acta Mater. 46 (1998) 2983–3001.
[22] R. Kubo, The fluctuation-dissipation theorem, Rep. Prog. Phys. 29 (2002) 255–283.
[23] Y.S. Li, H.Y. Wang, J. Chen, S.G. Yang, P. Sang, H.L. Long, Temperature gradient driving interdiffusion interface and composition evolution in Ni-Al-Cr alloys, Rare Met. 41 (2022) 3186–3196.
[24] J.C. Wang, M. Osawa, T. Yokokawa, H. Harada, M. Enomoto, Modeling the microstructural evolution of Ni-base superalloys by phase field method combined with CALPHAD and CVM, Comp. Mater. Sci. 39 (2007) 871–879.
[25] Y.S. Li, W.J. Zhao, X. Chen, P. Sang, Y.F. Ju, Phase-field simulation of evolution kinetics of second γ' phase in Ni-Al alloy under tensile stress, J. Mater. Res. Technol. 17 (2022) 1450–1458.
[26] A.T. Dinsdale, SGTE data for pure elements, Calphad 15 (1991) 317–425.
[27] I. Ansara, N. Dupin, H.L. Lukas, B. Sumdman, Thermodynamic assessment of the AlNi system, J. Alloy Compd. 247 (1997) 20–30.
[28] S.Y. Hu, L.Q. Chen, A phase-field model for evolution microstructures with strong elastic inhomogeneity, Acta Mater. 49 (2001) 1879–1890.
[29] D. Wang, Y.S. Li, S.J. Shi, X.W. Tong, Z.W. Yan, Phase-field simulation of γ' precipitates rafting and creep property of Co-base superalloys, Mater. Design 196 (2020), 109077.
[30] A.J. Ardell, The effects of elastic interactions on precipitate microstructural evolution in elastically inhomogeneous nickel-base alloys, Philos. Mag. A 94 (2014) 2101–2130.
[31] Y.H. Wen, B. Wang, J.P. Simmons, Y. Wang, A phase-field model for heat treatment applications in Ni-based alloys, Acta Mater. 54 (2006) 2087–2099.
[32] R.H. Wu, Z.F. Yue, M. Wang, Effect of initial γ/γ' microstructure on creep of single crystal nickel-based superalloys: a phase-field simulation incorporating dislocation dynamics, J. Alloys Compd. 779 (2019), 326–334.
[33] L.Q. Chen, J. Shen, Applications of semi-implicit Fourier-spectral method to phase field equations, Comput. Phys. Commun. 108 (1998) 147–158.
[34] J.C. Wang, M. Osawa, T. Yokokawa, H. Harada, M. Enomoto, Phase-field Modeling with CALPHAD and CVM for Microstructural Evolution of Ni-Base Superalloy, TMS, 2004.
[35] N. Zhou, C. Shen, M.J. Mills, Y. Wang, Contributions from elastic inhomogeneity and from plasticity to γ' rafting in single-crystal Ni–Al, Acta Mater. 56 (2008) 6156–6173.
[36] D.Y. Li, L.Q. Chen, Shape evolution and splitting of coherent particles under applied stresses, Acta Mater. 47 (1999) 247–257.
[37] H. Mughrabi, U. Tetzlaff, Microstructure and high-temperature strength of monocrystalline nickel-base superalloys, Adv. Eng. Mater. 2 (2000) 319–326.
[38] H. Feng, H. Biermann, H. Mughrabi, Microstructure-based 3D finite element modelling of lattice misfit and long-range internal stresses in creep−deformed nickel-base superalloy single crystals, Mat. Sci. Eng. A. 214 (1996) 1–16.
[39] F.R.N. Nabarro, Rafting in superalloys, Metall. Mater. Trans. A. 27 (1996) 513–530.
[40] S. Socrate, D.M. Parks, Numerical determination of the elastic driving force for directional coarsening in Ni-superalloys, Acta Metall. Mater. 41 (1993) 2185–2209.
[41] Z.G. Mao, C.K. Sudbrack, K.E. Yoon, G. Martin, D.N. Seidman, The mechanism of morphogenesis in a phase-separating concentrated multicomponent alloy, Nat. Mater. 6 (2007) 210–216.
[42] H.L. Huang, G.Q. Liu, H. Wang, Dissolution behavior and kinetics of γ' phase during solution treatment in powder metallurgy nickel-based superalloy, Metall. Mater. Trans. A. 51 (2019) 1075–1084.
[43] O.T. Ola, O.A. Ojo, M.C. Chaturvedi, Effect of deformation mode on hot ductility of a γ' precipitation strengthened nickel-base superalloy, Mat. Sci. Eng. A. 585 (2013) 319–325.
[44] C. Woodward, W.A. Vand, M. Asta, D.R. Trinkle, First-principles study of interfacial boundaries in Ni-Ni_3Al, Acta Mater. 75 (2014) 60–70.
[45] K.E. Yoon, R.D. Noebe, D.N. Seidman, Effects of rhenium addition on the temporal evolution of the nanostructure and chemistry of a model Ni–Cr–Al superalloy I: Experimental observations, Acta Mater. 55 (2007) 1145–1157.

[46] P.K. Rastogi, A.J. Ardell, The coherent solubilities of γ' in Ni–Al, Ni–Si and Ni–Ti alloys, Acta Metall. 17 (1969) 595–602.
[47] E.Y. Plotnikov, Z.G. Mao, R.D. Noebe, D.N. Seidman, Temporal evolution of the γ(fcc)/γ'($L1_2$) interfacial width in binary Ni–Al alloys, Scripta Mater. 70 (2014) 51–54.
[48] D.L. Shu, S.G. Tian, L.R. Liu, B.S. Zhang, N. Tian, Elements distribution and deformation features of a 4.5% Re nickel-based single crystal superalloy during creep at high temperature, Mater. Charact. 141 (2018) 433–441.